Decomposition of coherent and incoherent phonon conduction in superlattices and random multilayers

Yan Wang, Haoxiang Huang, and Xiulin Ruan*

School of Mechanical Engineering and Birck Nanotechnology Center, Purdue University, West Lafayette, Indiana 47907, USA

(Received 19 February 2014; revised manuscript received 15 August 2014; published 6 October 2014)

Nonequilibrium molecular dynamics (NEMD) simulations on conceptual binary Lennard-Jones systems show that the thermal conductivity (κ) of a superlattice (SL) can be significantly reduced by randomizing the thicknesses of its layers, by which a SL becomes a random multilayer (RML). Such reduction in κ is a clear signature of coherent phonon that can be localized in RMLs. We build a two-phonon model that divides the overall heat conduction into coherent and incoherent phonon contributions. In SL both coherent and incoherent phonons contribute to heat conduction, while in RML coherent phonons are localized so only incoherent phonons contribute. This model can fit the length dependence of the thermal conductances predicted in our NEMD simulations very well. The ballistic-limit thermal conductance and the intrinsic mean free path (MFP) of both coherent and incoherent phonons, and the localization length of coherent phonons, are obtained by fitting our model to the NEMD simulation results. The significant increase in κ of SL with total length is due to the long MFP of coherent phonons, and the lower κ of RML than SL is caused by the localization of coherent phonons.

DOI: 10.1103/PhysRevB.90.165406 PACS number(s): 66.70.−f, 63.20.Pw, 68.65.Cd, 68.65.Ac

I. INTRODUCTION

Phonon transport in the cross-plane direction of a superlattice (SL) may manifest particle-like or wave-like characteristics depending on how far a phonon can travel coherently without losing its phase information [1]. If phase breaking happens quickly, for instance, before a phonon traverses one period (L_p) of the SL, both the phonon propagation within each layer and the transmission/reflection at each individual interface will be similar to those in a single-interface heterojunction regardless of the SL structure. One such case is when the phases of phonons are randomized at rough interfaces [2]. In this case, phonons are incoherent and can be treated as particles. In contrast, if a phonon can transport coherently over a distance of several L_p's, phonon interference due to multiple reflections at the periodic interfaces leads to new phonon spectra. In such case, phonon transport is coherent and the wave nature of phonons should be considered. It should be noted that the terms "coherent" and "ballistic" correspond to the phase and momentum of a phonon, respectively, and are not necessarily equivalent. Detailed comparison between them can be found in Ref. [2].

Extensive efforts have been made to develop SLs for thermoelectric applications, where a low lattice thermal conductivity (κ) is essential for achieving a high figure of merit [3–6]. One benefit of the SL structure is the feasibility to tune its κ by controlling L_p or the interface conditions, e.g., roughness and species mixing. In the particlelike regime, κ increases with increasing L_p due to the reduced density of interfaces. In contrast, in the wavelike regime κ decreases with increasing L_p due to reduced group velocities and enlarged band gaps [7,8]. The coexistence of these two opposite trends, i.e., κ first decreases and then increases with increasing L_p in a single κ-L_p curve, has been observed in experiments and numerical studies [9–15], and the minimum κ was proposed as a signature of the transition from the wave regime to the particle regime as L_p increases [9]. However, κ was found to increase monotonically with increasing L_p in most experiments [16–18], implying a predominance of incoherent phonon transport (or particle regime). The presence of interface roughness or species mixing was proposed to cause the absence of the coherent phonon transport (or wave regime) [11,19,20], and these defects were also seen as opportunities for reducing the κ of SLs [11,21].

The properties of specific coherent phonon modes have been measured experimentally [22–24], while the importance of coherent phonons to the overall thermal transport has only recently been addressed by Luckyanova *et al.*'s experiment [2]. In their paper, κ was found to increase almost linearly with the total length of GaAs/AlAs SLs at 30–297 K, which was attributed to coherent phonon conduction. The trend that κ increases with increasing SL length has been observed in previous molecular dynamics simulations [13,19,20,25,26], but little attention was paid to the role played by coherent phonons. It is reasonable to expect that coherent phonons are the dominant heat carriers in long SLs as those in Luckyanova *et al.*'s experiment, and mechanisms that suppress the transport of coherent phonons should be effective in reducing κ. The transport of various other types of waves, e.g., electron and photon, can be substantially suppressed in disordered systems due to Anderson localization [27–30]. The localization of phonons in low-dimensional disordered media was also studied [31–39], however inadequate attention was paid to the overall thermal transport properties of 3D systems [40–43].

In terms of computational approaches, previous studies have treated phonons either completely incoherently [44–47] or coherently [7,9,12,14,48–50]. Taking a binary SL composed of alternating layers of material A and B as an example, the incoherent treatment assumes that all phonons traverse distinct A and B layers successively and transmit/reflect at the A/B or

*ruan@purdue.edu

B/A interfaces in the same way as a single interface between two semi-infinite A and B. In contrast, the coherent approach acquires phonon properties from the superlattice phonon spectra corresponding to a large unit cell (UC) composed of one layer of A and one layer of B. Evidently, both methods have their own drawbacks. The incoherent approach cannot explain some observations that κ may decrease with increasing L_p, while the coherent treatment contradicts the fact that the phase-breaking length, or the coherence length (L_ϕ) of some phonons may be comparable to or shorter than L_p. A more accurate description of phonons in SL should consider the coexistence of both incoherent phonons that retain the properties of A and B materials and have short L_ϕ in terms of L_p, and coherent ones possessing properties arising from the new large UC of the SL and can travel without phase breaking over a distance of several L_p's.

In this paper we investigate the thermal transport in binary SLs and random multilayers (RML), i.e., alternating A and B layers of random thickness, using nonequilibrium molecular dynamics (NEMD) simulations. Perfect SL and RML are an ideal pair of systems for isolating the contributions of coherent and incoherent phonons to heat transfer. With the same total length and average layer thickness, SL and RML should have approximately the same scattering rate of incoherent phonons due to the same interface density, while coherent phonons may be localized in long RMLs and thereby their contribution to κ can be neglected. As a consequence, the κ of long RMLs are almost solely contributed by incoherent phonons, and the difference between $\kappa_{\rm SL}$ and $\kappa_{\rm RML}$ reveals the κ contributed by coherent phonons in SL. Indeed our results indicate that RML is an effective structure to localize the coherent phonons and reduce thermal conductivity. We also build a two-phonon model to consider the coexistence of coherent and incoherent phonons, and the model can successfully explain the NEMD results and extract the properties of these phonons. This paper is organized as follows. In Sec. II we describe the model system and the setup of our NEMD simulations. Then we present the NEMD simulation results and our two-phonon model in Sec. III. Finally, we conclude this paper in Sec. IV.

II. METHODOLOGY

A. Model system

Figure 1(a) shows binary model structures composed of 50% $m40$ atoms and 50% $m90$ atoms, which have atomic mass of $m_A = 40.0$ g/mol and $m_B = 90.0$ g/mol, respectively. The model structures are constructed by the stacking of face-centered-cubic UCs along the [100] direction. We first consider two semi-infinite solids with a single interface, which will give the diffusive limit of the interfacial resistance. The total length of the system is up to 2.2 μm. The SL is created from periodic repetition of $m40$ and $m90$ layers of constant thickness d_{m40} and d_{m90}. Accordingly, $d = d_{m40} = d_{m90}$ and $L_p = 2d$ for the SLs studied in this paper. If the thicknesses of $m40$ and $m90$ layers are totally randomized [51], a SL becomes a RML. A SL and a RML with the same d have the same interface density.

The $m40$-$m90$ model structures mentioned above are conceptual atomic systems, in which the interatomic interactions are modeled by the Lennard-Jones (LJ) potential,

$$\phi_{ij}(r_{ij}) = 4\epsilon\left[\left(\frac{\sigma}{r_{ij}}\right)^{12} - \left(\frac{\sigma}{r_{ij}}\right)^{6}\right], \tag{1}$$

where ϕ_{ij} and r_{ij} are the pairwise interaction potential energy and the distance between atoms i and j, and σ and ϵ are the zero-potential-energy pair separation and the potential well depth, respectively. LJ systems have been widely used in conceptual studies owing to their lower computational cost than many other potential forms, as well as the simplicity in independently controlling the lattice constant (by σ) and the interatomic interaction strength (by ϵ). The parameter set of $\sigma_{\rm Ar} = 0.34$ nm, $\epsilon_{\rm Ar} = 0.0104$ eV, and a cutoff radius of $2.5\sigma_{\rm Ar}$ have been adopted in previous studies on solid argon [49,52]. In this paper, we use $\epsilon = 16\epsilon_{\rm Ar}$ for the interaction between all atoms, i.e., $m40$-$m40$, $m40$-$m90$, and $m90$-$m90$, to mimic materials like Si/Ge and GaAs/AlAs which have much stronger bonding than solid argon. The zero-potential-energy pair separation and the cutoff radius are $\sigma_{\rm Ar}$ and $2.5\sigma_{\rm Ar}$.

We conduct lattice dynamics calculations using the GULP package [53] to compute the phonon dispersions of the $m40$ and $m90$ crystals, and a $m40$-$m90$ SL which is built from alternating layers of 1 UC thick $m40$ and 1 UC thick $m90$ (1UC + 1UC) and a 2UC + 2UC SL. As shown in Fig. 1(b), the phonon bands are flatter in the SL than in $m40$ and $m90$ crystals, and SL with thicker layers (2UC + 2UC) has flatter bands than that with thinner layers (1UC + 1UC).

B. Simulation setup

The simulation domain setup is shown in Fig. 1(c). The device of length L is sandwiched between two heat baths of length $L_{\rm bath}$. About 1 nm thick of atoms (the dark regions) at the two ends are frozen to work as the fixed boundary condition (bc). We leave two 8.4 nm long buffer regions between the device and each of the two heat baths to extract the temperature at the two ends of the device, i.e., T_L and T_R. We use $\Delta t =$ 1 fs as the simulation time step based on the criteria given in Ref. [52], that is, $\Delta t \approx 0.002\sqrt{\sigma^2 m/\epsilon}$.

Our NEMD simulations (at temperature T) are conducted with the LAMMPS package [54] in the following process. (1) The periodic bc is applied to all three directions (X as the length direction, Y and Z as the lateral directions) and each atom is given a random velocity vector based on the Gaussian distribution function with a mean of 0 and a variance corresponding to a temperature of 5 K. (2) The entire supercell is relaxed in the NPT ensemble at zero pressure, and the temperature increases gradually from 5 K to T in 200 ps. (3) The entire supercell is relaxed in the NPT ensemble at zero pressure and temperature T for 300 ps. (4) About 1 nm layer of atoms at both ends of the supercell are frozen and kept so, which is equivalent to applying the fixed bc to the X direction. (5) NEMD simulation is performed where the velocities of the atoms in the two heat baths are rescaled to a temperature of $T + \Delta T/2$ or $T - \Delta T/2$ every simulation step and the atoms in the fixed boundary regions are frozen. Step (5) lasts 10–40 ns depending on the length of the supercell to ensure that the heat current reaches steady state. Longer supercells need longer time to reach steady state.

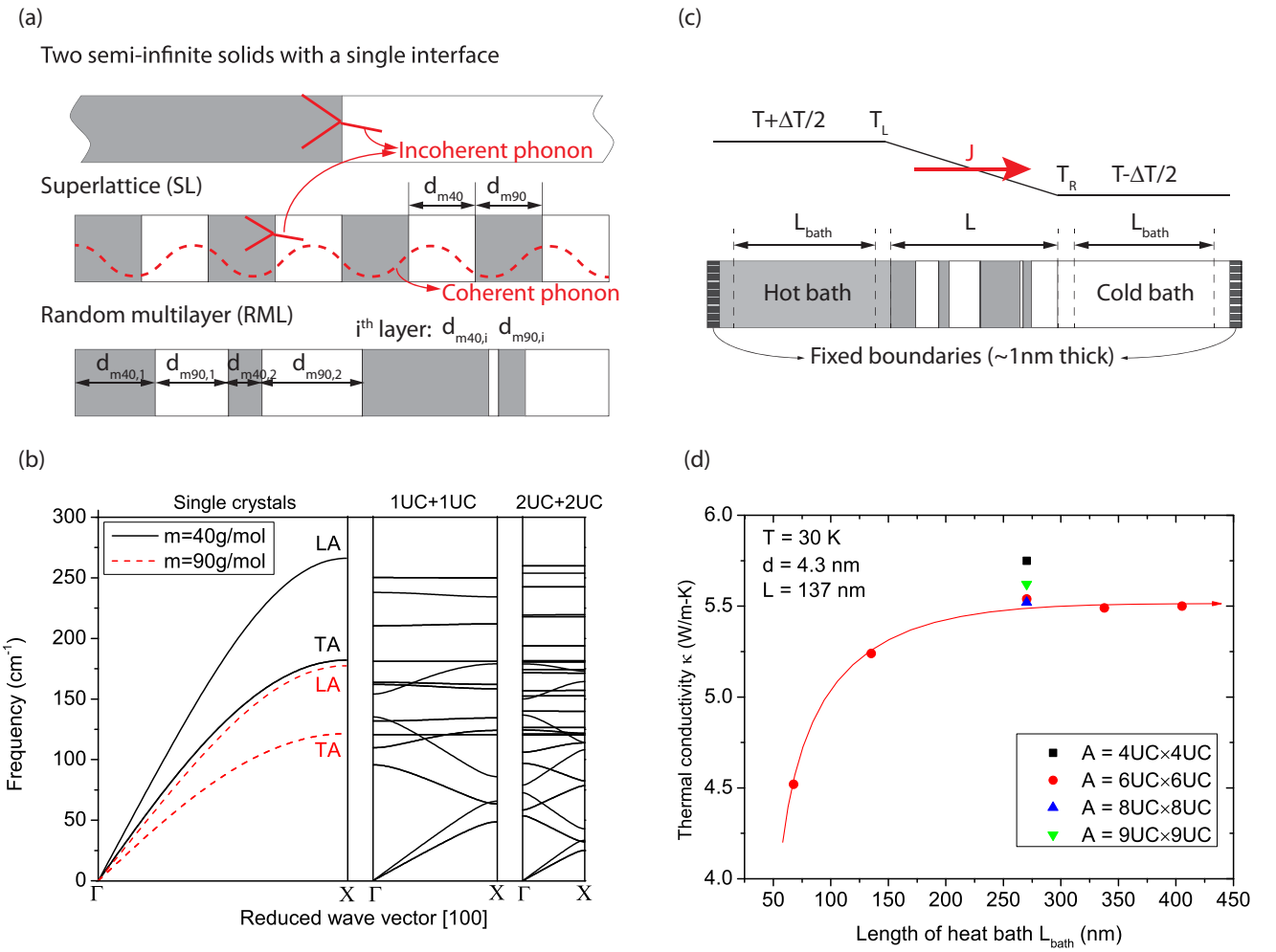

FIG. 1. (Color online) (a) Schematic of two semi-infinite solids with a single interface, superlattice (SL) and random multilayer (RML) made of alternating layers of $m40$ and $m90$. In single-interface systems phonons can be treated as incoherent particles, while in SLs phonons may manifest as either coherent waves or incoherent particles. The SL has uniform layer thickness $d_{m40} = d_{m90}$, while d_{m40} and d_{m90} are randomized in RML. In both SL and RML, there are 50% $m40$ and 50% $m90$ atoms. (b) Phonon dispersion relations along the [100] direction for: $m40$ and $m90$ crystals (left panel), 1UC × 1UC SL (center panel), and 2UC × 2UC SL (right panel). (c) Schematic of the simulation domain setup in this work. L_{bath} is the length of the heat bath and L is the total length of the device. The hot (cold) bath is maintained at $T + \Delta T/2(T - \Delta T/2)$. T_L and T_R are the steady-state local temperature at the buffer regions next to the two ends of the device. J is the steady-state heat current. (d) Convergence of predicted κ with respect to heat bath length L_{bath} and cross-sectional area A.

The thermal conductance G of the system is computed as $G = J/[A(T_L - T_R)]$, where A is the cross-sectional area of the device and J is the steady-state heat current, i.e., the amount of kinetic energy artificially injected into (extracted from) the hot (cold) heat bath per unit time. Then κ can be calculated as $\kappa = GL$. Quantification of the uncertainty in our simulations can be found in the Appendix.

C. Convergence study

Figure 1(d) shows the effect of heat bath length L_{bath} and cross-sectional area A on the thermal conductivity prediction for a SL with $L = 137$ nm and $d = 4.3$ nm at $T = 30$ K. Notably, the predicted κ increases with L_{bath} and saturates when $L_{\text{bath}} = 270.2$ nm. Beyond these lengths, κ does not depend on the length of the heat bath and they are used in our simulations. We use $A = 6$ UC $\times$ 6 UC as the cross-sectional area. Another scheme for NEMD calculation of κ is by applying a constant heat current and measuring the resulting ΔT, which has been used in previous studies on SLs [20,26,52,55]. The κ predicted from this method is $\kappa = 5.43$ W/m-K when $L_{\text{bath}} = 270.2$ nm and $A = 6$ UC $\times$ 6 UC, and the measured ΔT is approximately 5.4 K, which is in good agreement with the constant ΔT scheme used by us.

III. RESULTS AND DISCUSSIONS

A. Temperature distributions and thermal boundary resistances in SL and RML

Figures 2(a)–2(d) show the temperature profiles (dots) out of our NEMD simulations and the derived thermal boundary resistance R_i (crosses) of individual interfaces. R_i is computed as $R_i = A\Delta T_i/J$ and plotted with respect to the right y axis, where ΔT_i is the temperature drop at the ith interface. The diffusive-limit thermal boundary resistance R_s is obtained

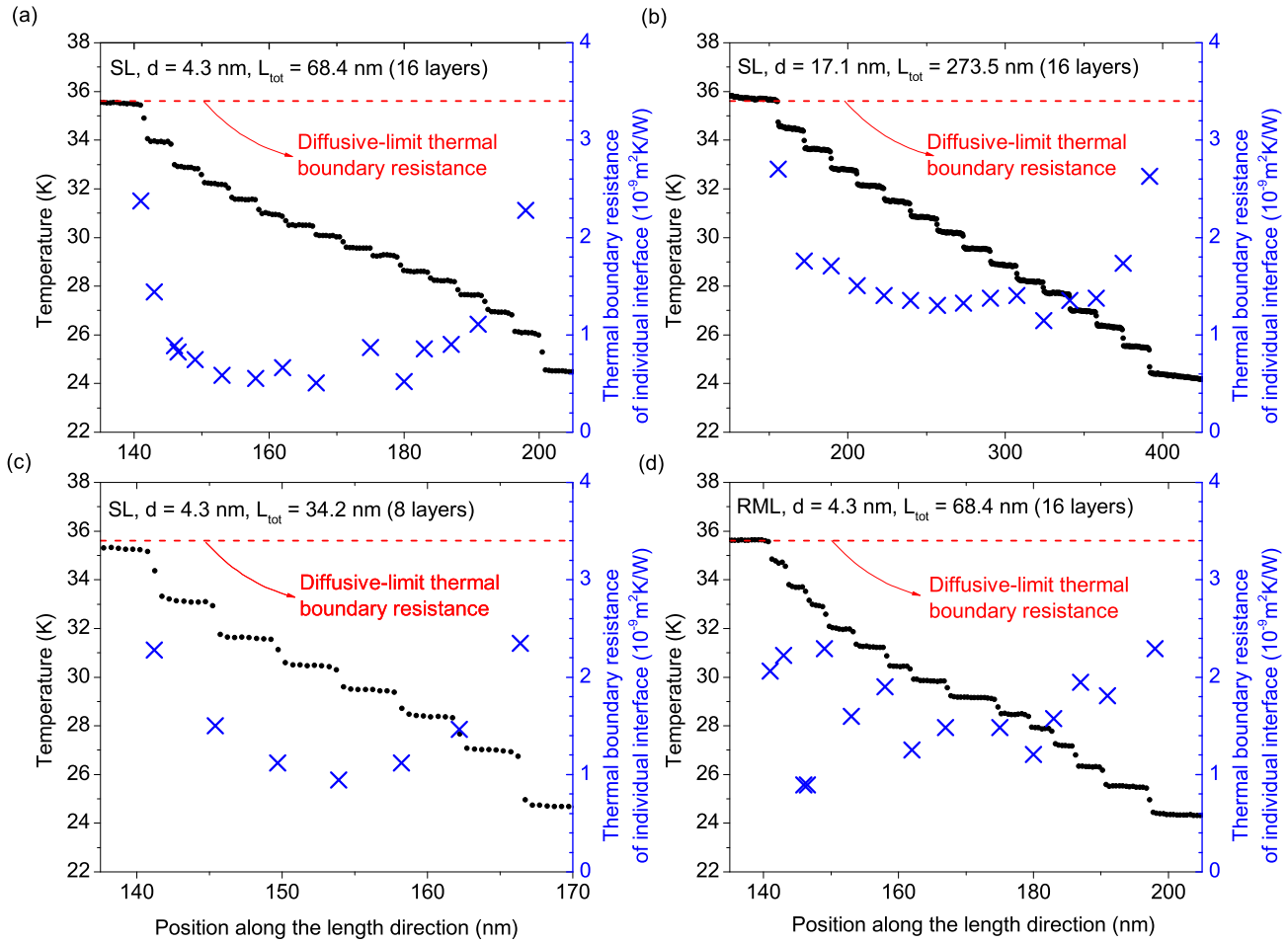

FIG. 2. (Color online) Temperature profiles (left y axis) and the thermal boundary resistances of each individual interface (right y axis) for: (a) a SL with $d = 4.3$ nm and $L = 68.4$ nm; (b) a SL with $d = 17.1$ nm and $L = 273.5$ nm; (c) a SL with $d = 4.3$ nm and $L = 34.2$ nm; (d) a RML with $d = 4.3$ nm and $L = 68.4$ nm. The red dashed lines show the diffusive limit of the thermal boundary resistance, i.e., 3.4×10^{-9} m^2K/W.

from NEMD simulations on single-interface heterojunctions of $m40$ and $m90$ crystals (see Supplemental Material [56]). In Figs 2(a)–2(d), the interfacial R's in SL and RML are lower than the diffusive limit R_s of $3.4 \times 10^{-9} m^2$K/W. Figure 2(a) (for a SL with $d = 4.3$ nm) and Fig. 2(b) (for a SL with $d = 17.1$ nm) reveal that R_i's are generally higher in SLs with thicker layers. Similar behaviors were observed in Si/Ge systems, where a thin Si (or Ge) film was sandwiched between two Ge (or Si) substrates [8]. This is a clear indication that the interfaces are coupled in SL of short period, and coherent thermal transport has to be considered. Also, in Fig. 2(a) we can see that R_i is almost constant ($R_i \approx 0.7 \times 10^{-9}$ m^2K/W) in the central region of the SL, but $R_i \approx 2.4 \times 10^{-9}$ m^2K/W for the interfaces at the end of the SL (closest to the heat baths). Similar observations have been made by Samvedi and Tomar on Si/Ge SLs, and the higher R of the interfaces closest to the heat baths was attributed to the filtering of phonons that originate from the heat bath but are not coherent in the SL, i.e., not following the phonon dispersion of the SL [25]. In SLs with many periods, R decreases from the ends to the center and levels off as shown in Figs. 2(a) and 2(b), while in short SLs, R may keep decreasing till the center of the SL, as shown in Fig. 2(c). Therefore, longer SLs should show stronger coherent phonon characteristics than shorter SLs.

Comparing Figs. 2(a) and Fig. 2(d), which are for a SL and a RML, respectively, we can see that R's of the interfaces in the RML are generally higher than those in the corresponding SL. This implies that both coherent and incoherent phonons transfer heat in the SL, while coherent ones are localized in the RML and only incoherent phonons contribute, leading to higher R's in RML. More in-depth analysis is given below.

B. Thermal conductance and thermal conductivity

The thermal conductance G and thermal conductivity κ of SLs (solid squares) and RMLs (solid circles) are predicted using the temperature profiles from NEMD simulations, and the results are shown in Figs. 3(a) and 3(b). Both the SLs and RMLs have $d = 4.3$ nm and the simulations are conducted at $T = 30$ K. We can see that G_{SL} and κ_{SL} are always higher than G_{RML} and κ_{RML}, respectively, indicating RMLs as a promising structure for applications such as thermoelectrics which requires low κ. In Fig. 3(b), κ_{SL} increases with L and saturates slowly, which agrees with the experiment by

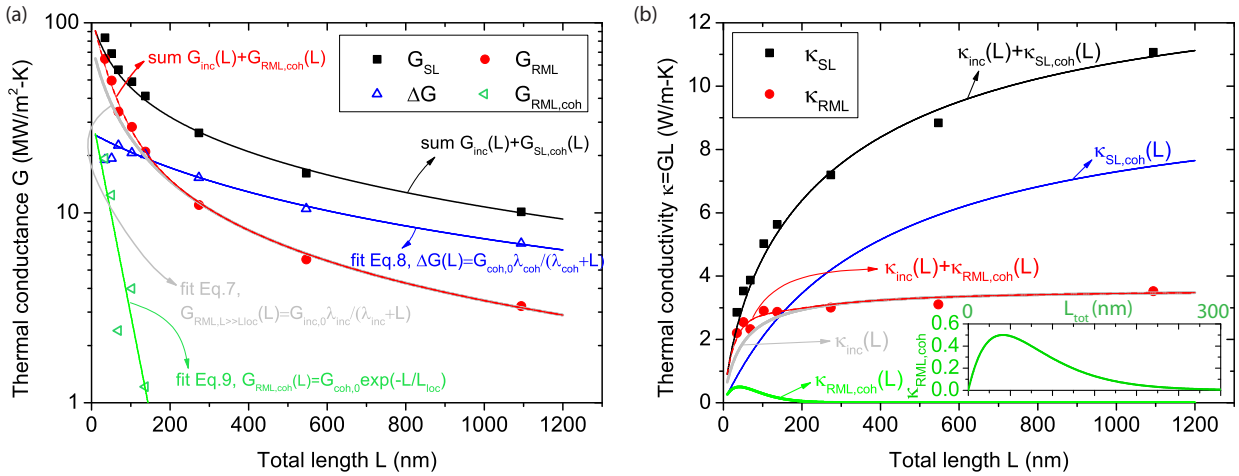

FIG. 3. (Color online) (a) Fitting of simulation data ($d = 4.3$ nm and $T = 30$ K) using the two-phonon model depicted by Eqs. (4)–(8). (b) Thermal conductivity $\kappa = GL$ as a function of L. The inset shows the zoom view of $k_{\rm coh}$ in RMLs for $L < 300$ nm. In both figures, markers are from simulations while curves are from model fitting.

Luckyanova *et al.* [2]; in contrast, $\kappa_{\rm RML}$ saturates much earlier than $\kappa_{\rm SL}$. Such a difference between SL and RML cannot be explained by only considering incoherent or ballistic phonon transport, since the average interface density is the same. Therefore, we believe the different behaviors of coherent phonons in SL and RML are responsible for such difference. In the following section, we will propose a two-phonon model to explain our simulation results.

C. Two-phonon model

Previous studies on SLs either treat all phonons as incoherent particles possessing properties of individual layers or as coherent waves with properties determined by the superlattice phonon spectra. Herein we propose a more general model that accounts for the coexistence of coherent and incoherent phonons in one system. In such a two-phonon model, we divide all phonon modes into two groups: coherent ones which are localizable in RML and incoherent ones which can be scattered at the interfaces in both SL and RML. In terms of the phonon spectrum, coherent phonons are the phonon modes with long wavelength and mean free path, while incoherent phonons are those with short wavelength and mean free path.

Within the Landauer framework, the thermal conductance depends on the device length L by [57]

$$G(L) = G_0 \frac{\lambda}{\lambda + L}, \tag{2}$$

where the subscript 0 indicates ballistic-limit quantity, so G_0 is the ballistic-limit thermal conductance, and λ is the phonon mean free path (MFP). Accordingly, the thermal conductivity κ is

$$\kappa(L) = G(L)L = G_0 \frac{\lambda L}{\lambda + L}, \tag{3}$$

which indicates that κ increases almost linearly with the total length when $L \ll \lambda$ (ballistic regime) while it saturates at a constant value when $L \gg \lambda$ (diffusive regime). Such a relation has been employed for phonon transport to compute the κ of silicon and Bi_2Te_3, and good agreement with experiment was achieved [58,59].

By treating coherent phonons and incoherent phonons as two lumped groups, the thermal conductance G of a SL can be expressed as

$$\begin{aligned} G_{\rm SL}(L) &= G_{\rm SL,coh}(L) + G_{\rm inc}(L) \\ &= G_{\rm coh,0} \frac{\lambda_{\rm coh}}{\lambda_{\rm coh} + L} + G_{\rm inc,0} \frac{\lambda_{\rm inc}}{\lambda_{\rm inc} + L}, \end{aligned} \tag{4}$$

where the subscripts coh and inc denote coherent and incoherent phonon, respectively.

In a random medium, e.g., RML, the Anderson localization of coherent energy carriers would lead to exponential decay of G when L increases. Noting that such localization acts on coherent phonons only, we modify the first term in Eq. (4) to include an exponential decay,

$$\begin{aligned} G_{\rm RML}(L) &= G_{\rm RML,coh}(L) + G_{\rm inc}(L) \\ &= G_{\rm coh,0} \frac{\lambda_{\rm coh}}{\lambda_{\rm coh} + L} \exp\left(-\frac{L}{L_{\rm loc}}\right) + G_{\rm inc,0} \frac{\lambda_{\rm inc}}{\lambda_{\rm inc} + L}, \end{aligned} \tag{5}$$

where $L_{\rm loc}$ is the localization length which describes how fast G decays in random media. In Eq. (5), we have assumed that the properties of both coherent and incoherent phonons (G_0 and λ) stay the same as those in SLs except that coherent phonons are localized in RMLs [60]. When L is large, the exponential term in Eq. (5) can be neglected as it decays much faster than the second term on the right hand side, i.e., coherent phonon contribution is negligible. Therefore,

$$G_{{\rm RML},L \gg L_{\rm loc}}(L) \approx G_{\rm inc}(L) = G_{\rm inc,0} \frac{\lambda_{\rm inc}}{\lambda_{\rm inc} + L}. \tag{6}$$

If we define $\Delta G(L) = G_{\rm SL} - G_{\rm RML}$, then for $L \gg L_{\rm loc}$, subtracting Eq. (6) from Eq. (4) gives

$$\Delta G(L)_{L \gg L_{\rm loc}} = G_{\rm SL,coh}(L) = G_{\rm coh,0} \frac{\lambda_{\rm coh}}{\lambda_{\rm coh} + L}. \tag{7}$$

For short RMLs, the G contributed by coherent phonons may be significant, which can be obtained by subtracting Eq. (6) from Eq. (5),

$$G_{\mathrm{coh,RML}}(L) = G_{\mathrm{coh},0}\frac{\lambda_{\mathrm{coh}}}{\lambda_{\mathrm{coh}}+L}\exp\left(-\frac{L}{L_{\mathrm{loc}}}\right). \quad (8)$$

D. Decomposition of thermal conductance

In Fig. 3(a), we fit our NEMD simulation results ($d =$ 4.3 nm and $T = 30$ K) with Eqs. (4)–(8). To distinguish discrete data points from fitted curves, in Fig. 3(a) and the following discussions, we denote the curves as functions of L, namely, $G_{\mathrm{inc}}(L)$, $G_{\mathrm{RML},L\gg L_{\mathrm{loc}}}(L)$, $\Delta G(L)$, $G_{\mathrm{SL,coh}}(L)$, and $G_{\mathrm{SL}}(L)$, while those without a trailing "(L)" indicate discrete data points. The model fitting is conducted in the following manner.

(1) Equation (6) is used to fit G_{RML} (solid circles) in the range of $L > 200$ nm to get $G_{\mathrm{inc},0}$ and λ_{inc}. We enforce $L >$ 200 nm since a proper use of Eq. (6) requires $L \gg L_{\mathrm{loc}}$. With $G_{\mathrm{inc},0}$ and λ_{inc}, we can back calculate $G_{\mathrm{inc}}(L)$ for the entire L range, not limited to $L > 200$ nm.

(2) The data points for ΔG (open up-triangles) are obtained by subtracting G_{RML} from G_{SL} (solid squares). Equation (7) is then used to fit ΔG in the $L > 200$ nm range to get $G_{\mathrm{coh},0}$ and λ_{coh}. Then the curve $\Delta G(L)$ can be obtained for the entire L range.

(3) Subtracting the $G_{\mathrm{inc}}(L)$ curve obtained in step (1) from G_{RML}, we can obtain a series of data points $G_{\mathrm{RML,coh}}$ (left-pointing triangles) decaying exponentially. We can get L_{loc} by fitting $G_{\mathrm{RML,coh}}$ with Eq. (8). Then we can obtain the curve $G_{\mathrm{RML,coh}}(L)$.

(4) According to Eq. (4), the summation of $G_{\mathrm{SL,coh}}(L)$, which is the $\Delta G(L)$ obtained in step (2), and the $G_{\mathrm{inc}}(L)$ obtained in step (1) gives $G_{\mathrm{SL}}(L)$, and the result [the dark line indicated as $G_{\mathrm{inc}}(L) + G_{\mathrm{SL,coh}}(L)$ in Fig. 3(a)] agrees well with the G_{SL} (solid squares) predicted by our simulations (dark squares), again demonstrating the applicability of our two-phonon model to multilayer structures. It is worth mentioning that in Fig. 3(b) and its inset, $\kappa_{\mathrm{RML,coh}}(L)$ first increases with L and then decreases. The increase is due to ballistic phonon transport (κ increases with L in ballistic transport regime) while the decrease is due to phonon localization.

Using the above fitting procedure, we fit our two-phonon model to three sets of simulation data obtained from independent simulations with different initial conditions and RML configurations. Figure 4(a) shows the ballistic-limit thermal conductance G_0 as a function of d for coherent and incoherent phonons. Notably, $G_{0,\mathrm{coh}}$ decreases quickly with increasing d. This is because the phonon group velocity decreases with increasing d due to zone folding, which has been illustrated in previous lattice dynamics studies [7,61]. Figure 4(b) shows λ_{coh} and λ_{inc} in SLs (left y axis), and L_{loc} of coherent phonons in RMLs (right y axis). We can see that λ_{inc} increases significantly with increasing d, which arises from decreased density of interfaces that hinder the forward propagation of incoherent phonons. Also, λ_{coh} is always larger than λ_{inc}. This is because the interfaces are lattice discontinuities for incoherent phonons while they are not "seen" by coherent phonons. L_{loc} also

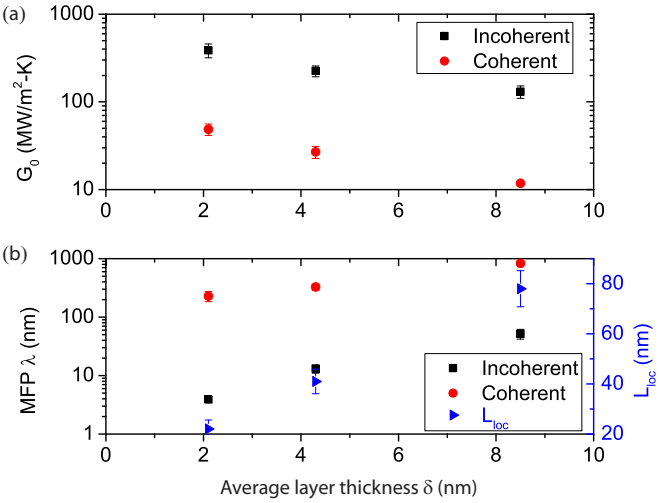

FIG. 4. (Color online) (a) Ballistic-limit thermal conductance G_0 of coherent and incoherent phonons in SLs; (b) MFP λ of coherent phonons and incoherent phonons in SLs and the localization length L_{loc} of coherent phonons in RMLs.

increases with d, but it is shorter than 80 nm for all the d's we studied. Therefore, the contribution of coherent phonons to G_{RML} is negligible in RMLs with $L > 200$ nm, and the validity of step (1) of the above fitting procedure is confirmed. We need to point out that here we have used a single L_{loc} for the group of coherent and localized phonon modes in RML, but in principle each coherent mode can have its own L_{loc}, so $G_{\mathrm{RML,coh}}$ do not necessarily decay exactly exponentially.

Now if we revisit Fig. 3(b) with Fig. 4 in mind, we can gain the following insights: (1) The fact that κ_{SL} increases with L reflects a ballistic transport behavior of coherent phonons which have long MFP. (2) κ_{RML} is lower than κ_{SL} due to the localization of coherent phonons in RML. (3) The fact that κ_{RML} saturates quickly with increasing L reflects a diffusive behavior of incoherent phonons which have short MFP.

E. Relative importance of coherent phonons as a function of temperature and layer thickness

To quantify the importance of the contribution of coherent phonons, we plot κ of SL and RML, as well as their difference $\Delta\kappa = \kappa_{\mathrm{SL}} - \kappa_{\mathrm{RML}}$ as a function of temperature, and the results are shown in Figs. 5(a) and 5(b). We can see that $\Delta\kappa$ decreases as T rises, indicating that coherent phonons become less important at higher T. Similarly, Figs. 6(a) and 6(b) show κ and $\Delta\kappa$ as a function of d for $T = 30$ K and $T = 100$ K, respectively. Apparently, $\Delta\kappa$ also decreases with increasing d, indicating that coherent phonons become less important at larger d.

To explain this trend, note that we have argued in Sec. I that coherent phonons are important only if the coherence length L_ϕ of phonons extends several d's so that enough phonon interferences can occur to form the SL phonon spectra; otherwise the phonons manifest themselves as incoherent particles. To support this argument, we explore the correlation between $\Delta\kappa$ and L_ϕ/d. $\Delta\kappa$ quantifies coherent phonon contribution to heat

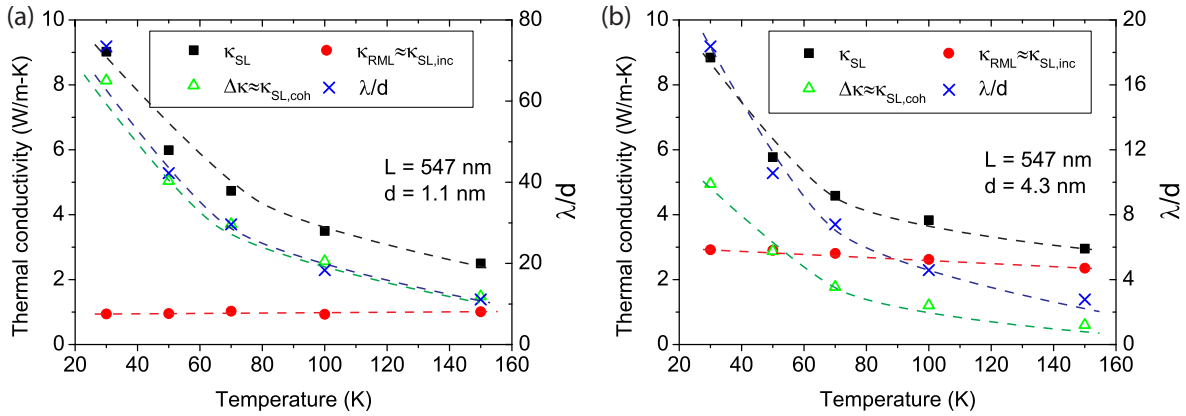

FIG. 5. (Color online) Thermal conductivity of SL and RML, and the difference between them as a function of temperature T (left Y-axis). The ratio of MFP λ to average layer thickness d as a function of T (right Y-axis). (a) is for $d = 1.1$ nm and (b) is for $d = 4.3$ nm. The dashed curves are guides for the eyes.

conduction, and L_ϕ/d specifies how many layers a phonon can traverse coherently, and we anticipate a positive correlation between them. Since L_ϕ is inconvenient to evaluate, we approximate it to be λ. In pristine bulk crystalline materials, L_ϕ is related to both the normal and Umklapp processes since they are both inelastic and thereby can break the phase of phonons, while λ is related only to the Umklapp process since it causes thermal resistance (momentum breaking) [62]. Nevertheless L_ϕ and λ are positively correlated and λ is easier to obtain in NEMD simulations (details can be found in the Appendix).

In Figs. 5(a) and 5(b), we indeed see that both $\Delta\kappa$ and λ/d decrease as T rises. In Figs. 6(a) and 6(b), we also see that both $\Delta\kappa$ and λ/d decrease with increasing d. Clearly, higher T (which leads to higher inelastic scattering rate and shorter λ) or larger d will lead to smaller λ/d, meaning that there is a higher chance of phase-breaking scattering before a phonon traverses each layer. Therefore, the coherent phonon contribution $\Delta\kappa$ decreases. The extreme case is when T is so high or d is so large that most phonons have lost their phase before traversing a layer and, consequently, $\kappa_{SL} = \kappa_{RML}$. In addition, κ_{RML} increases substantially with increasing d owing to decreased interface density. A similar trend was also reported for SLs with interface mixing or roughness, indicating a predominance of incoherent phonons [20,44].

In addition, we can clearly see a minimum κ_{SL} with respect to d, which is due to the competition of coherent and incoherent phonons per the discussions above. The coherent phonon contribution $\kappa_{SL,coh}$ decreases with d, due to the fast decrease in $G_{0,coh}$ owing to reduced group velocities. On the other hand, $\kappa_{SL,inc}$ increases with d due to the increase in λ_{inc} owing to the reduced interface density. Since κ_{SL} is a summation of $\kappa_{SL,coh}$ and $\kappa_{SL,inc}$, a minimum $\kappa_{SL,min}$ can form at a critical layer thickness d_c. Below d_c, the effect of coherent phonons dominates so κ_{SL} decreases with d. Above d_c, the effect of incoherent phonons dominates so κ_{SL} increases with d.

IV. CONCLUSIONS

To summarize, we have conducted NEMD simulations on conceptual binary Lennard-Jones systems and proposed a two-phonon model to interpret the simulation results for SLs and RMLs. Our model considers the coexistence of coherent and incoherent phonon contribution to heat conduction in SLs and RMLs, and can fit the simulation data very well. κ_{SL} and κ_{RML} were found to increase with the total length of

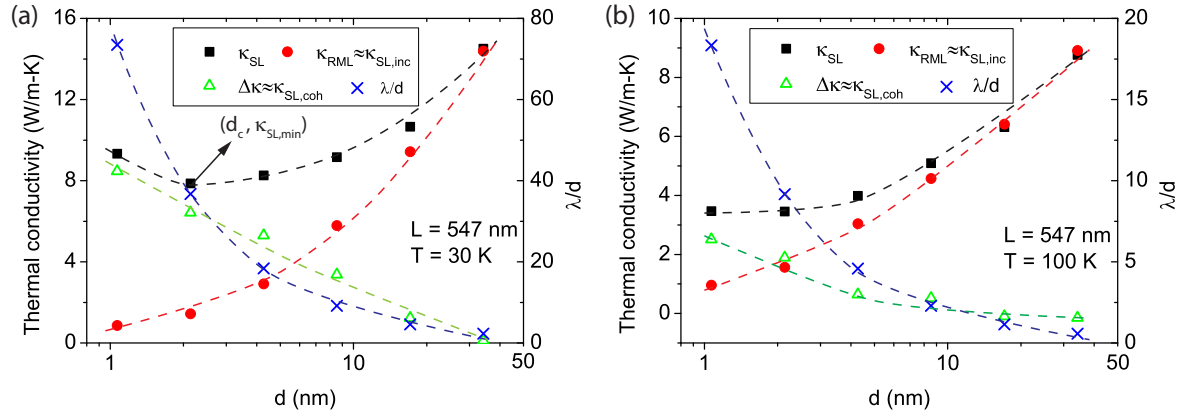

FIG. 6. (Color online) Thermal conductivity of SL, RML and the difference between them as a function of d (left Y-axis). The ratio of MFP λ to average layer thickness d as a function of d (right Y-axis). (a) and (b) are for $T = 30$ K and $T = 100$ K, respectively. The dashed curves are guides for the eyes.

the structure, while $\kappa_{RML} < \kappa_{SL}$ and κ_{RML} saturates at a finite value much sooner than κ_{SL}. We attribute the increasing κ with total length in SLs to coherent phonon transport, and the lower κ of RML than SL to the localization of coherent phonons due to the random layer thickness. Using the two-phonon model, we also extracted the phonon MFP and ballistic-limit thermal conductance of coherent phonons and incoherent phonons. Based on our findings, we propose RMLs as low-κ materials that may be used for thermoelectric applications.

As a final remark, we note that as the current model considers all coherent and incoherent phonons as two gray media, the fact that different phonon modes can have different MFP and wavelength is significantly neglected, and the nonequilibrium between phonons [63] are not considered. A possible extension of our model would be a spectral treatment of phonon modes. Besides, when metal layers are involved, electron-phonon scattering can also considerably destroy the phase of phonons, and electron-phonon nonequilibrium near the interface can also play a role in determining the thermal transport properties [64].

ACKNOWLEDGMENTS

The authors are grateful to the financial support from the Air Force Office of Scientific Research (AFOSR) and National Science Foundation (NSF).

APPENDIX A: SIMULATION UNCERTAINTY

To quantify the uncertainty associated with our NEMD simulations, we conduct 48 independent simulations for SLs with 16 layers (SL-16L), RMLs with 16 layers (RML-16L), SLs with 64 layers (SL-64L), and RMLs with 64 layers (RML-64L), of which the average layer thickness is $d = 4.3$ nm. The histogram of the computed κ's normalized by their average are shown in Fig. 7. The uncertainty is defined as the standard deviation of κ normalized by the average κ, and is found to be 2.2%, 5.7%, 2.3%, and 3.8% for SL-16L, RML-16L, SL-64L, and RML-64, respectively. There are several sources of uncertainty in our NEMD simulations. For SLs, the uncertainty comes from the statistical nature of molecular dynamics, where the difference in initial conditions and process can lead to slightly different results. However, a RML can have different configurations due to the many possible arrangements of d_i's for given L and d. Such variation in d_i's may add to the uncertainty. As we can see in Fig. 7 as well as the normalized

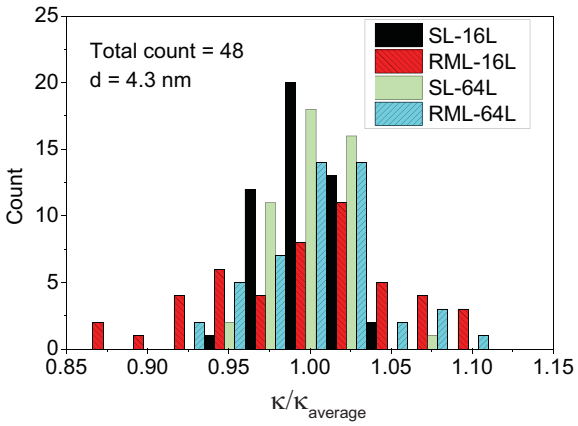

FIG. 7. (Color online) Histogram of κ normalized by the corresponding average for 48 independent samples for SLs with 16 layers (SL-16L), RMLs with 16 layers (RML-16L), SLs with 64 layers (SL-64L), and RMLs with 64 layers (RML-64L), of which $d = 4.3$ nm and $T = 30$ K.

standard deviations mentioned above, the simulated κ's of RMLs are more dispersed than those of SLs. The uncertainty is even larger for RMLs with less layers (RML-16L) than those with more layers (RML-64L), since there is a higher chance that RML-64L is fully randomized than RML-16L.

APPENDIX B: ESTIMATING λ

We estimate the average group velocity as

$$\overline{v}^{-1} = \frac{v_{LA}^{-1} + 2v_{TA}^{-1}}{3}, \tag{B1}$$

which considers the longitudinal acoustic branch (subscript LA) and the two degenerate transverse acoustic branches (TA). λ can be estimated from $\lambda = 3\kappa/(c\overline{v})$. Here c is the classical heat capacity of the LJ crystal, which is $c = 3k_B n$ with k_B denoting the Boltzmann constant and n the atom number density. The lattice constant a of the LJ crystal is (5.278 ± 0.008) Å in the temperature range studied here (30–150 K), so $n = 4/a^3 \approx 2.72 \times 10^{28}\, m^{-3}$ and hence $c = 1.13 \times 10^6 \mathrm{J/m^3} - \mathrm{K}$. v_{LA} and v_{TA} are estimated as the Brillouin zone center group velocity of the corresponding branches in Fig. 1(b), and we get $v_{LA,m40} = 4135$ m/s, $v_{TA,m40} = 3053$ m/s, $v_{LA,m90} = 2748$ m/s, and $v_{TA,m90} = 2039$ m/s. The κ's of $m40$ and $m90$ crystals are computed from NEMD simulations and Green-Kubo calculations of which the details can be found in the Supplemental Material [56]. Finally, the average λ of $m40$ and $m90$ crystals are taken as $\lambda^{-1} = \lambda_{m40}^{-1} + \lambda_{m90}^{-1}$.

[1] G. Chen, *Nanoscale Energy Transport and Conversion: A Parallel Treatment of Electrons, Molecules, Phonons, and Photons* (Oxford University Press, USA, 2005).
[2] M. N. Luckyanova, J. Garg, K. Esfarjani, A. Jandl, M. T. Bulsara, A. J. Schmidt, A. J. Minnich, S. Chen, M. S. Dresselhaus, Z. Ren, E. A. Fitzgerald, and G. Chen, Science **338**, 936 (2012).
[3] R. Venkatasubramanian, E. Siivola, T. Colpitts, and B. O'quinn, Nature (London) **413**, 597 (2001).
[4] T. Harman, P. Taylor, M. Walsh, and B. LaForge, Science **297**, 2229 (2002).
[5] H. Boettner, G. Chen, and R. Venkatasubramanian, MRS Bulletin **31**, 211 (2006).
[6] I. Chowdhury, R. Prasher, K. Lofgreen, G. Chrysler, S. Narasimhan, R. Mahajan, D. Koester, R. Alley, and R. Venkatasubramanian, Nat. Nanotechnol. **4**, 235 (2009).

[7] S.-i. Tamura, Y. Tanaka, and H. J. Maris, Phys. Rev. B **60**, 2627 (1999).

[8] E. Landry and A. McGaughey, J. Appl. Phys. **107**, 013521 (2010).

[9] M. V. Simkin and G. D. Mahan, Phys. Rev. Lett. **84**, 927 (2000).

[10] R. Venkatasubramanian, Phys. Rev. B **61**, 3091 (2000).

[11] B. C. Daly, H. J. Maris, K. Imamura, and S. Tamura, Phys. Rev. B **66**, 024301 (2002).

[12] B. Yang and G. Chen, Phys. Rev. B **67**, 195311 (2003).

[13] Y. Chen, D. Li, J. R. Lukes, Z. Ni, and M. Chen, Phys. Rev. B **72**, 174302 (2005).

[14] J. Garg and G. Chen, Phys. Rev. B **87**, 140302 (2013).

[15] J. Ravichandran, A. K. Yadav, R. Cheaito, P. B. Rossen, A. Soukiassian, S. J. Suresha, J. C. Duda, B. M. Foley, C.-H. Lee, Y. Zhu, A. W. Lichtenberger, J. E. Moore, D. A. Muller, D. G. Schlom, P. E. Hopkins, A. Majumdar, R. Ramesh, and M. A. Zurbuchen, Nat. Mater **13**, 168 (2014).

[16] S.-M. Lee, D. G. Cahill, and R. Venkatasubramanian, Appl. Phys. Lett. **70**, 2957 (1997).

[17] W. S. Capinski, H. J. Maris, T. Ruf, M. Cardona, K. Ploog, and D. S. Katzer, Phys. Rev. B **59**, 8105 (1999).

[18] S. T. Huxtable, A. R. Abramson, C.-L. Tien, A. Majumdar, C. LaBounty, X. Fan, G. Zeng, J. E. Bowers, A. Shakouri, and E. T. Croke, Appl. Phys. Lett. **80**, 1737 (2002).

[19] K. Imamura, Y. Tanaka, N. Nishiguchi, S. Tamura, and H. Maris, J. Phys.: Condens. Matter **15**, 8679 (2003).

[20] E. S. Landry and A. J. H. McGaughey, Phys. Rev. B **79**, 075316 (2009).

[21] K. Termentzidis, S. Merabia, P. Chantrenne, and P. Keblinski, Int. J. Heat Mass Transfer **54**, 2014 (2011).

[22] V. Narayanamurti, H. L. Störmer, M. A. Chin, A. C. Gossard, and W. Wiegmann, Phys. Rev. Lett. **43**, 2012 (1979).

[23] C. Colvard, R. Merlin, M. V. Klein, and A. C. Gossard, Phys. Rev. Lett. **45**, 298 (1980).

[24] Y. Wang, X. Xu, and R. Venkatasubramanian, Appl. Phys. Lett. **93**, 113114 (2008).

[25] V. Samvedi and V. Tomar, Nanotechnology **20**, 365701 (2009).

[26] K.-H. Lin and A. Strachan, Phys. Rev. B **87**, 115302 (2013).

[27] P. W. Anderson, Phys. Rev. **109**, 1492 (1958).

[28] M. Kohmoto, B. Sutherland, and K. Iguchi, Phys. Rev. Lett. **58**, 2436 (1987).

[29] W. Gellermann, M. Kohmoto, B. Sutherland, and P. C. Taylor, Phys. Rev. Lett. **72**, 633 (1994).

[30] X. Ruan and M. Kaviany, Microscale Thermophys. Eng. **9**, 63 (2005).

[31] K. Ishii, Prog. Theor. Phys. Suppl. **53**, 77 (1973).

[32] S. Tamura and J. P. Wolfe, Phys. Rev. B **36**, 3491(R) (1987).

[33] N. Nishiguchi, S.-i. Tamura, and F. Nori, Phys. Rev. B **48**, 14426 (1993).

[34] N. Nishiguchi, S.-i. Tamura, and F. Nori, Phys. Rev. B **48**, 2515 (1993).

[35] W. Frizzera, G. Viliani, M. Montagna, A. Monteil, and J. Capobianco, J. Phys.: Condens. Matter **9**, 10867 (1997).

[36] E. Maciá, Phys. Rev. B **61**, 6645 (2000).

[37] R. Curbelo-Blanco, F. de León-Pérez, R. Pérez-Alvarez, and V. R. Velasco, Phys. Rev. B **65**, 172201 (2002).

[38] Y. Wang, B. Qiu, and X. Ruan, Appl. Phys. Lett. **101**, 013101 (2012).

[39] Y. Wang, A. Vallabhaneni, J. Hu, B. Qiu, Y. P. Chen, and X. Ruan, Nano Lett. **14**, 592 (2014).

[40] P. Schelling and S. Phillpot, J. Appl. Phys. **93**, 5377 (2003).

[41] A. Frachioni and B. White, J. Appl. Phys. **112**, 014320 (2012).

[42] J. D. Bodyfelt, M. C. Zheng, R. Fleischmann, and T. Kottos, Phys. Rev. E **87**, 020101 (2013).

[43] A. Bermudez, M. Bruderer, and M. B. Plenio, Phys. Rev. Lett. **111**, 040601 (2013).

[44] G. Chen, Phys. Rev. B **57**, 14958 (1998).

[45] A. Pattamatta and C. K. Madnia, Int. J. Heat Mass Transfer **52**, 860 (2009).

[46] D. Singh, J. Y. Murthy, and T. S. Fisher, J. Heat Transfer **133**, 122401 (2011).

[47] Z. Aksamija and I. Knezevic, Phys. Rev. B **88**, 155318 (2013).

[48] A. Ward and D. A. Broido, Phys. Rev. B **77**, 245328 (2008).

[49] S. C. Huberman, J. M. Larkin, A. J. H. McGaughey, and C. H. Amon, Phys. Rev. B **88**, 155311 (2013).

[50] I. O. Thomas and G. P. Srivastava, Phys. Rev. B **88**, 115207 (2013).

[51] A RML is created from the corresponding SL in the following way: (1) randomly select a layer thicker than 1 UC; (2) move 1 UC thick of this layer to another randomly chosen layer of the same material; (3) repeat the above steps for $100 \times N$ times, where N is the number of layers.

[52] E. S. Landry, M. I. Hussein, and A. J. H. McGaughey, Phys. Rev. B **77**, 184302 (2008).

[53] J. D. Gale, J. Chem. Soc., Faraday Trans. **93**, 629 (1997).

[54] S. Plimpton, J. Comput. Phys. **117**, 1 (1995).

[55] K. Termentzidis, P. Chantrenne, and P. Keblinski, Phys. Rev. B **79**, 214307 (2009).

[56] See Supplemental Material at http://link.aps.org/supplemental/10.1103/PhysRevB.90.165406 for NEMD and Green-Kubo results of the thermal conductivity of $m40$ and $m90$ at different temperatures .

[57] S. Datta, *Quantum transport: atom to transistor* (Cambridge University Press, New York, US, 2005).

[58] C. Jeong, S. Datta, and M. Lundstrom, J. Appl. Phys. **109**, 073718 (2011).

[59] C. Jeong, S. Datta, and M. Lundstrom, J. Appl. Phys. **111**, 093708 (2012).

[60] This is reasonable considering that with the same d and L, SL and RML have the same number of interfaces (for interface scattering of phonons) and total thickness of $m40$ and $m90$ layers (for internal scattering of phonons). Therefore, the scattering rates of incoherent phonons should be approximately the same in SL and RML.

[61] P. Hyldgaard and G. D. Mahan, Phys. Rev. B **56**, 10754 (1997).

[62] When there is roughness or other types of defect, which are usually more momentum-breaking than phase-breaking, L_ϕ can be comparable to or longer than the MFP λ (Ref. [1]).

[63] X. Wu and T. Luo, J. Appl. Phys. **115**, 014901 (2014).

[64] Y. Wang, X. Ruan, and A. K. Roy, Phys. Rev. B **85**, 205311 (2012).